Supplement of Atmos. Chem. Phys., 19, 15503–15531, 2019
https://doi.org/10.5194/acp-19-15503-2019-supplement

Supplement of

Complex refractive indices and single-scattering albedo of global dust aerosols in the shortwave spectrum and relationship to size and iron content

Claudia Di Biagio et al.

Correspondence to: Claudia Di Biagio (claudia.dibiagio@lisa.u-pec.fr)

Calculation of the size distribution behind SW instruments inlets

The size distribution sensed by SW optical instruments, i.e. that behind the SW optical instruments inlets $(dN/dlogD_g)_{SWoptics}$, was calculated started from the size in CESAM. To do so, the particle loss functions in the sampling lines for the nephelometer and the aethalometer were calculated as a function of particle diameter ($L_{neph}(D_g)$, $L_{aeth}(D_g)$) using the Particle Loss Calculator (PLC, von der Weiden et al., 2009) using as input the geometry of the sampling line, the sampling flow rate, the particle shape factor, and the particle density. The uncertainty on calculated loss functions was estimated with a sensitivity study by varying in the PLC software values of the input parameters within their estimated uncertainties.

As shown in Fig. S1, the loss functions agree within uncertainties for the nephelometer and the aethalometer in the entire diameter range, meaning that the same dust size distribution is sensed by the two instruments. An average loss function ($L_{SWoptics}(D_g)$) between that of the nephelometer and the aethalometer was calculated and used to estimate a common $(dN/dlogD_g)_{SWoptics}$ as:

$$\left[\frac{dN}{dlogD_g}\right]_{SWoptics} = \left[\frac{dN}{dlogD_g}\right]_{CESAM}\left(1-L_{SWoptics}\left(D_g\right)\right) \quad (1).$$

Fig S1. Particle loss function versus particle geometric diameter ($L(D_g)$) calculated for the WELAS OPC, the nephelometer, the aethalometer, and the filter sampling inlets by using the Particle Loss Calculator software (von der Weiden et al., 2009). The uncertainty on calculated loss functions was estimated with a sensitivity study by varying in the PLC software values of the input parameters within their estimated uncertainties.

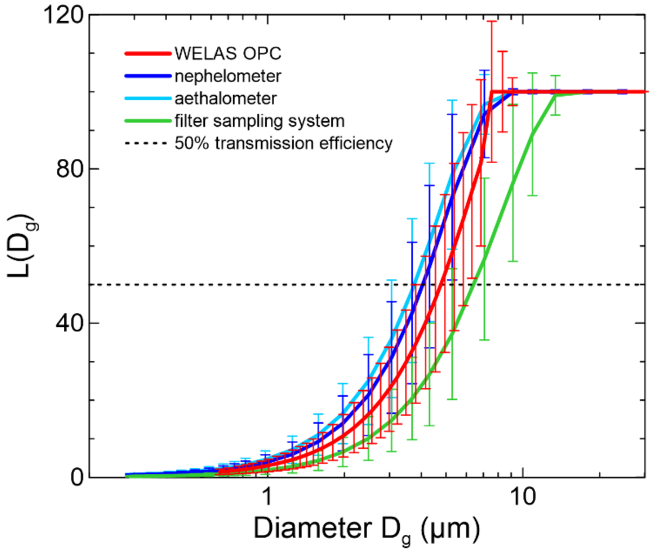

Lognormal fitting parameters of the dust size distribution

The dust size distribution $(dN/dlogD)_{SWoptics}$ measured at each 10–min time step for each sample was fitted with a sum of five lognormal functions. For each mode the parameters of the lognormal functions, i.e. the total number concentration (N_i), the geometric median diameter ($D_{g,i}$), and the geometric standard deviation of the distribution (σ_i), were retrieved. The uncertainty on the retrieved parameters were estimated by repeating the fits by using size data within their uncertainties. The central parameters of the lognormal fitting of $(dN/dlogD_g)_{SWoptics}$ at the peak of the injection are reported in Table S1 while an example of the multimodal fit for four dust samples are shown in Fig. S2. The average geometrical diameter and standard deviation for the five modes are very similar between the nineteen different samples, so that the same modes contribute to the dust size. The relative proportion of the modes nonetheless largely changes from sample to sample, suggesting that different soils are more or less prone to generate different aerosol size fractions. It also changes with time for each given sample, in particular with the decrease of the largest modes due to gravitational settling in the chamber. The time– and sample–averaged D_g and σ (± their st.dev.) of the five modes are 0.26 (±0.04) and 1.53 (±0.08) for mode 1, 0.71 (±0.05) and 1.31 (±0.04) for mode 2, 1.47 (±0.11) and 1.30 (±0.02) for mode 3, 2.56 (±0.26) and 1.17 (±0.06) for mode 4, and 3.77 (±0.53) and 1.25 (±0.08) for mode 5. Note that the fit of field observations also usually requires four or five modes between 0.05 and 5.0 µm geometrical diameter (e.g., Osborne et al., 2008; Ryder et al., 2013a; Denjean et al., 2016a).

Figure S2. Example of multimodal lognormal fitting for four dust size distribution datasets measured behind the SW inlets during experiments with the Algeria, Mali, Patagonia, and Australia samples. Shown data are 10–min average data taken 20 minutes after dust aerosol injection in the CESAM chamber. The single modes contributing to the multimodal fit are shown in color. The multimodal fit obtained as the sum of the single modes is also shown (thick black line) together with the multimodal fits obtained by fitting data within plus or minus their error bars (dotted black lines). Fitted function were cut at 10 µm of diameters (the cutoff of the SW inlets) for subsequent utilization.

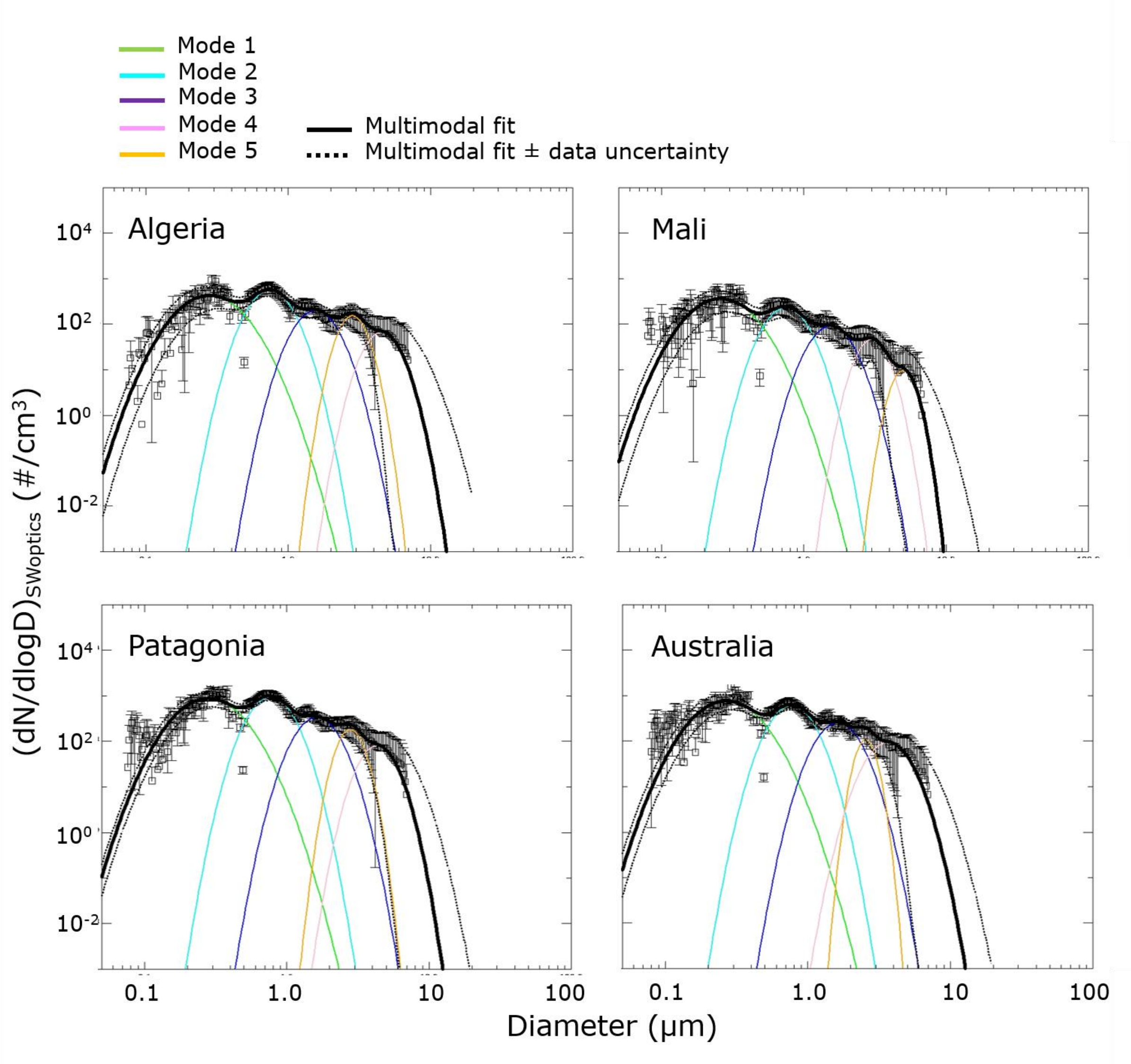

Figure S3. Example of correlation between scattering and absorption coefficients measured at the wavelengths of 470, 520, and 950 nm for Morocco dust sample. The linear fits are also shown, and the retrieved parameters of the fit and correlation coefficient (R^2) are also indicated in the plot.

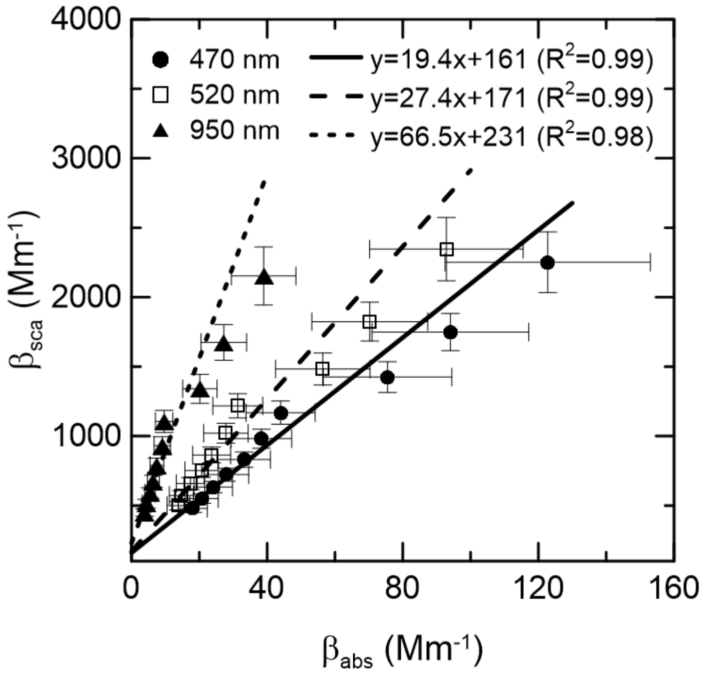

Figure S4. Control experiment with ammonium sulphate particles. Left panel: temporal evolution of the scattering (β_{sca}) coefficient measured in the chamber by the nephelometer at 450, 550, and 700 nm. Right panel: spectral attenuation (β_{ATT}) measured by the aethalometer and derived absorption coefficient (β_{abs}) at the peak of ammonium sulphate particles injection.

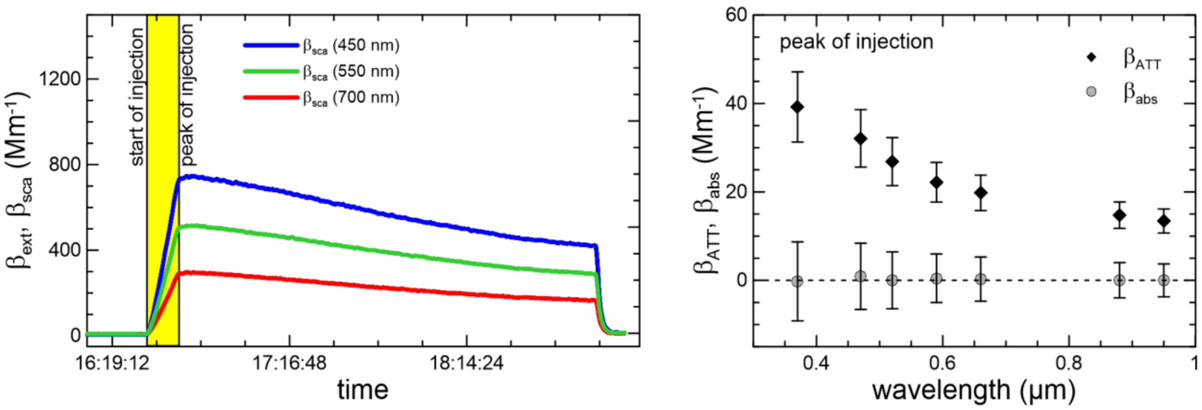

Table S1 Parameters (total number concentration N_i, in no. cm^{-3}, geometric median diameter $D_{g,i}$ in µm, and geometric standard deviation σ_i) for the five log-normal modes i used to parameterize the number size distributions at the peak of the dust injection in CESAM for the different dust samples.

	Mode 1			**Mode 2**			**Mode 3**			**Mode 4**			**Mode 5**		
	N	D_g	σ_i	N	D_g	σ_i	N	D_g	σ_i	N	D_g	σ_i	N	D_g	σ_i
Tunisia	1050	0.27	1.50	507	0.69	1.30	221	1.4	1.30	49	2.6	1.19	36	3.9	1.31
Morocco	342	0.28	1.50	260	0.75	1.30	104	1.5	1.30	54	2.8	1.23	13	4.8	1.20
Libya	527	0.27	1.50	445	0.73	1.30	158	1.5	1.30	23	2.4	1.11	67	3.3	1.29
Algeria	267	0.29	1.50	207	0.77	1.30	65	1.6	1.30	37	2.8	1.20	26	4.5	1.25
Mauritania	269	0.25	1.50	139	0.72	1.30	51	1.5	1.30	17	2.7	1.17	8	4.2	1.20
Niger	468	0.24	1.50	305	0.69	1.30	150	1.4	1.30	31	2.4	1.15	58	3.6	1.35
Mali	234	0.24	1.51	76	0.75	1.30	26	1.6	1.30	6	2.5	1.11	10	3.4	1.23
Bodélé	1967	0.34	1.50	828	0.85	1.30	319	1.7	1.30	129	2.8	1.19	189	4.3	1.35
Ethiopia	460	0.28	1.50	443	0.76	1.30	148	1.6	1.30	72	2.7	1.18	59	4.2	1.32
Saudi Arabia	652	0.29	1.50	440	0.79	1.30	102	1.7	1.30	4	2.0	1.30	61	3.3	1.31
Kuwait	283	0.24	1.56	126	0.71	1.30	50	1.5	1.30	19	2.8	1.19	10	4.3	1.35
Gobi	1061	0.25	1.50	456	0.67	1.30	161	1.4	1.30	28	2.6	1.17	23	3.9	1.31
Taklimakan	610	0.27	1.50	423	0.77	1.30	179	1.6	1.30	71	2.7	1.18	88	4.1	1.34
Arizona	1261	0.29	1.50	858	0.82	1.30	285	2.0	1.41	10	2.0	1.35	66	4.5	1.27
Atacama	1144	0.27	1.50	1278	0.78	1.30	514	1.6	1.30	149	2.6	1.17	142	3.8	1.30
Patagonia	526	0.27	1.50	353	0.78	1.30	113	1.7	1.30	47	2.8	1.20	28	4.5	1.25
Namib–1	665	0.29	1.50	394	0.79	1.30	124	1.7	1.30	52	2.9	1.17	57	4.2	1.32
Namib–2	496	0.26	1.50	291	0.77	1.30	76	1.7	1.30	21	2.6	1.13	34	3.7	1.30
Australia	483	0.27	1.50	224	0.79	1.30	77	1.6	1.30	23	2.6	1.13	35	3.8	1.30

Table S2. Ångstrom Absorption Exponent (AAE) calculated as the power-law fit of β_{abs} versus λ between 370 and 950 nm. Mean and standard deviations over experiments are reported for each soil.

Geographical area	Sample	AAE
Northern Africa – Sahara	Tunisia	2.0 ± 0.1
	Morocco	2.0 ± 0.2
	Libya	2.2 ± 0.1
	Algeria	2.3 ± 0.4
	Mauritania	2.2 ± 0.2
Sahel	Niger	1.7 ± 0.1
	Mali	1.5 ± 0.3
	Bodélé	2.3 ± 0.1
Eastern Africa and the Middle East	Ethiopia	2.2 ± 0.1
	Saudi Arabia	2.4 ± 0.1
	Kuwait	2.3 ± 0.3
Eastern Asia	Gobi	2.1 ± 0.1
	Taklimakan	2.0 ± 0.1
North America	Arizona	1.6 ± 0.2
South America	Atacama	1.8 ± 0.1
	Patagonia	2.2 ± 0.4
Southern Africa	Namib-1	2.1 ± 0.3
	Namib-2	2.0 ± 0.2
Australia	Australia	2.2 ± 0.2

References

Denjean, C., Cassola, F., Mazzino, A., Triquet, S., Chevaillier, S., Grand, N., Bourrianne, T., Momboisse, G., Sellegri, K., Schwarzenbock, A., Freney, E., Mallet, M., and Formenti, P.: Size distribution and optical properties of mineral dust aerosols transported in the western Mediterranean, Atmos. Chem. Phys., 16, 1081–1104, https://doi.org/10.5194/acp-16-1081-2016, 2016a.

Osborne, S.R., Johnson, B.T., Haywood, J.M., Baran, A.J., Harrison, M.A.J., and McConnell, C.L.: Physical and optical properties of mineral dust aerosol during the Dust and Biomass-burning Experiment, J. Geophys. Res., 113, D00C03, doi:10.1029/2007jd009551, 2008.

Ryder, C. L., Highwood, E. J., Rosenberg, P. D., Trembath, J., Brooke, J. K., Bart, M., Dean, A., Crosier, J., Dorsey, J., Brindley, H., Banks, J., Marsham, J. H., McQuaid, J. B., Sodemann, H., and Washington, R.: Optical properties of Saharan dust aerosol and contribution from the coarse mode as measured during the Fennec 2011 aircraft campaign, Atmos. Chem. Phys., 13, 303-325, doi:10.5194/acp-13-303-2013, 2013a.

von der Weiden, S.-L., Drewnick, F., and Borrmann, S.: Particle Loss Calculator – a new software tool for the assessment of the performance of aerosol inlet systems, Atmos. Meas. Tech., 2, 479–494, 2009.